Impact resistance of single-layer metallic glass nanofilms to high-velocity micro-particle penetration

J.L. Dong [a], X. Song [b,d], Z.J. Wang [c], K.L. Xiao [a,d], Y.H. Liu [c], G. Wilde [e], X.Q. Wu [a,*], M.Q. Jiang [b,d,**]

[a] *Key Laboratory of Mechanics in Fluid Solid Coupling Systems, Institute of Mechanics, Chinese Academy of Sciences, 100190 Beijing, China*
[b] *State Key Laboratory of Nonlinear Mechanics, Institute of Mechanics, Chinese Academy of Sciences, 100190 Beijing, China*
[c] *Institute of Physics, Chinese Academy of Sciences, 100190 Beijing, China*
[d] *School of Engineering Science, University of Chinese Academy of Sciences, 100049 Beijing, China*
[e] *Institute of Materials Physics, Westfälische Wilhelms-Universität Münster, 48149, Münster, Germany*

ABSTRACT

Macro- and microscale metallic glasses exhibit excellent protective capability under hypervelocity projectile impact conditions. However, it is formidably challenging to evaluate the ballistic performance of metallic glasses with characteristic sizes down to the nanoscale. Here, we adopt the laser-induced micro-particle impact technique to penetrate 60-nm-thick $Ni_{60}Ta_{40}$ metallic glass nanofilms with projectile velocities in the range of 186–540 m/s. Based on the ballistic analysis, the superior impact resistance of the metallic glass nanofilms is quantitatively characterized in terms of the specific penetration energy. The post-mortem observations of the penetration features reveal that shear-banding, cracking, and bending of cracking-induced petals are the main energy dissipation modes beyond the localized perforated hole, which is strongly dependent on impact velocities. This work for the first time achieves high-strain-rate loading on nanoscale metallic glasses, and extends their engineering applications as promising armor materials for high-velocity impact protection.

© 2021 Elsevier Ltd. All rights reserved.

1. Introduction

Improving the protective performance of materials subjected to hypervelocity impact is of paramount importance in a variety of both military and civilian applications involving bullet-proof body armor [1], debris-proof spacecraft shielding [2], etc. In recent decades, various impact-protective materials [3–14] have been developed, ranging from advanced alloys, carbon materials to nanostructured polymers. For example, 10–100 nm thick multilayer graphene shows excellent capability for impact energy dissipation under supersonic projectile penetration [5]. Cai and Thevamaran [6] have reported that the sub-100 nm thick semicrystalline P(VDF-TrFE) films are of very high specific penetration energy due to the combined effects of highly mobile polymer chains and the intermolecular dipole–dipole interactions. Metallic glasses (MGs) as a relatively young class of advanced alloys also exhibit high impact resistance due to their unique mechanical and physical properties [15–17]. Huang et al. [18] reported that

a Fe-based MG coating reinforced bumper in a Whipple shield structure could provide a higher protection level compared to the traditional one by producing a high shock pressure and an associated temperature rise in the projectile. Hofmann and co-workers [19–21] explored the hypervelocity impact behaviors of MGs and MG composites, and they found that compared to the Kevlar layers, the MG ribbons as intermediate layers in spacecraft Whipple shields could effectively improve the resistance to the hypervelocity impact of debris particles.

It is noted that in these pioneering work, the characteristic thickness of MGs along the impact direction resides in the range of tens of micrometers to several millimeters. An intriguing question therefore arises: if the characteristic thickness of MGs is reduced to tens of nanometers, at what level is their performance of impact resistance? It is well known that compared to macroscopic samples, MGs at the nanoscale usually show higher strength and larger ductility [22–26]. According to the quasistatic-regime mechanical properties, one could expect a superior impact resistance for nanoscale MGs. However, up to now, there is no direct experimental evidence to prove this fascinating expectation.

In this work, we conducted high-velocity micro-particle penetration into $Ni_{60}Ta_{40}$ MG nanofilms with a characteristic thickness of about 60 nm. Based on the ballistic analysis, the specific
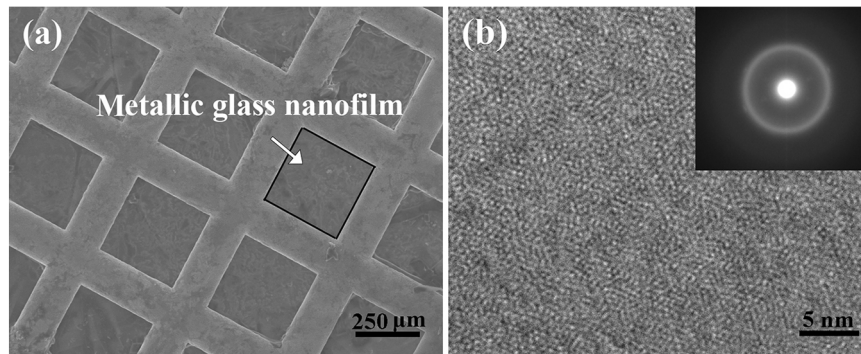
Fig. 1. (a) A low-magnification SEM image showing the $Ni_{60}Ta_{40}$ MG nanofilm supported by TEM copper grids. (b) A high-resolution TEM image of the nanofilm and the inset shows the corresponding SAED pattern.
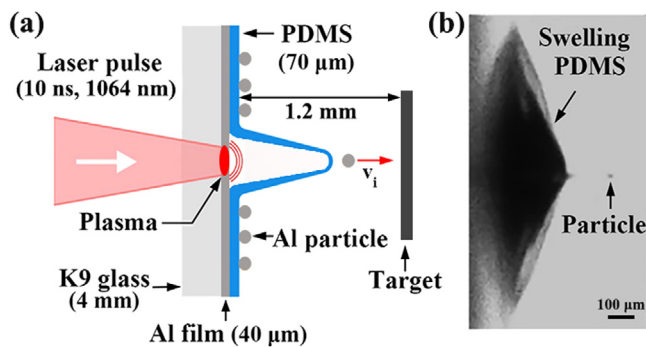

Fig. 2. (a) A schematics of the laser-induced micro-particle impact test platform adapted from [28]. (b) A snapshot shows the expanding PDMS film and a moving Al micro-particle.

penetration energy is analyzed to quantitatively evaluate the impact resistance of the MG nanofilms. The penetration features at different impact velocities are further examined to reveal the basic modes for energy dissipation during penetration. This study provides solid evidence that the $Ni_{60}Ta_{40}$ MG at the nanoscale shows an impact resistance performance comparable to that of the "armor-grade" Kevlar composite and some nanomaterials, significantly surpassing most bulk protective materials.

2. Materials and methods

A $Ni_{60}Ta_{40}$ MG nanofilm was chosen as the candidate material for impact protection, because its bulk sample shows ultrahigh strength of 3.5 GPa and excellent thermal stability [27]. The $Ni_{60}Ta_{40}$ MG nanofilms were prepared via ion beam assisted deposition (IBAD). An 80-nm-thick aluminum (Al) layer was initially deposited on a flat polycarbonate (PC) plate with a diameter of 10 cm, and then the $Ni_{60}Ta_{40}$ film with a thickness h of about 60 nm was deposited on the top surface of the Al layer by the IBAD method. The $Ni_{60}Ta_{40}$ MG nanofilm was detached from the PC substrate by dissolving the in-between Al layer with 1 mol/L NaOH solution. After that, the MG nanofilm was transferred to and attached firmly with 100 mesh transmission electron microscopy (TEM) cooper grids as the impact targets, as shown in Fig. 1a. Except for its periphery, the $Ni_{60}Ta_{40}$ nanofilm within a grid is free-standing and unsupported. Fig. 1b shows the high-resolution TEM image of the $Ni_{60}Ta_{40}$ MG nanofilm. The typical speckle pattern stemming from scattering at an amorphous structure is clearly observed, which is consistent with the featureless halo observed by selected-area electron diffraction (SAED) as shown in the inset.

In order to explore the impact-resistance performance of the $Ni_{60}Ta_{40}$ MG nanofilm, we build a laser-induced micro-particle impact test (LIPIT) platform, as illustrated in Fig. 2a. The LIPIT technique was originally developed by Lee et al. [5,29] and further improved by Veysset et al. [28] and Hassani-Gangaraj et al. [30, 31]. The launch pad of the LIPIT consists of a 4-mm-thick K9 glass substrate, a 40-μm-thick Al film, and a 70-μm-thick polydimethylsiloxane (PDMS) film (from left to right). The microparticles are dispersed on the free surface of the PDMS. A single laser pulse excited by a Q-switched Nd:YAG laser with 10 ns duration and 1064 nm wavelength is focused into a 1-mm-diameter spot size on the Al film. The micro-particles are accelerated toward the target through fast expansion of the laser-induced plasma constrained between the K9 glass and the Al film and resultant rapid swelling of the PDMS film. We launch the spherical Al particles with a diameter D of 25 ± 2 μm (the supplementary material, Fig. S1) to impact the $Ni_{60}Ta_{40}$ MG nanofilms at various velocities. The impact process is *in-situ*, real-time captured by using a high-speed SIMD 16 camera with a NAVITAR microscope objective lens ($12\times$ magnification, 34-cm focal length). An AD 500 light-source (white full spectrum, 2-ms duration, 4-channel) is used for illumination. Depending on impact velocities of microparticles, the interframe time is adjusted from 50 to 300 ns, and the corresponding exposure time is from 20 to 100 ns. Fig. 2b presents a snapshot of the swelling PDMS film and a moving Al micro-particle.

3. Results and discussion

With the LIPIT platform, we carried out the micro-particle impact experiments at impact velocities ranging from 186 to 540 m/s, which are controlled by adjusting the laser pulse energy (from 0.25 to 0.45 J). The corresponding strain rates are up to $\sim 10^6$ s^{-1}. The calculation of the strain rate is provided in the supplementary material. For all impact velocities, the Al microparticle penetrated through the $Ni_{60}Ta_{40}$ MG nanofilm. Fig. 3 shows a typical penetration process at the highest impact velocity (540 m/s) recorded by the high-speed camera. Due to the penetration, there is a kinetic energy loss ΔE_k for the micro-particle that can be calculated by measuring its impact velocity v_i and residual velocity v_r,

$$\Delta E_k = \frac{1}{2} m \left(v_i^2 - v_r^2 \right), \tag{1}$$

where the mass of a micro-particle $m = (2.2 \pm 0.2) \times 10^{-11}$ kg. The data of v_i, v_r and ΔE_k for the eight impacts are provided in the supplementary material, Table S2.

Fig. 4a plots the kinetic energy loss ΔE_k versus the impact velocity v_i, and a positive correlation between the two quantities is clearly identified. During the present impacts, there are two
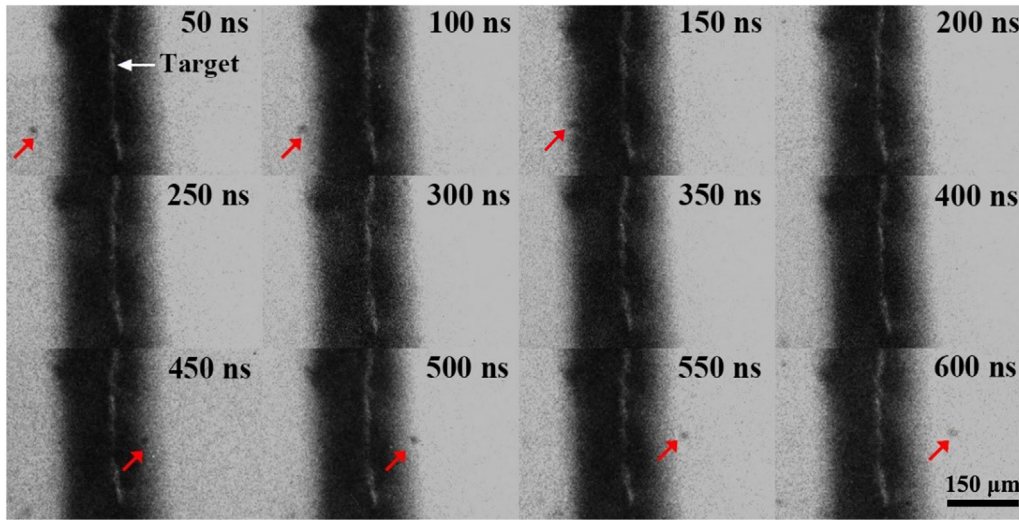
Fig. 3. Multi-frame snapshots (size: 580×380 µm^2) with 50 ns interframe time show that an Al micro-particle at 540 m/s penetrates through the Ni$_{60}$Ta$_{40}$ MG nanofilm.

contributions to ΔE_k: (1) the energy E_p that is used to penetrate the MG nanofilm, and (2) the energy dissipation E_{air} due to the air drag. The latter is determined by [5] $E_{air} = ma_{air}d$, where a_{air} is the deceleration by air drag and d is the travel distance of the micro-particle during a penetration event. Here, we choose $d \sim 190$ µm from the 150 ns to 450 ns snapshots in Fig. 3. We measure the a_{air} for the different impact velocities and then calculate the E_{air} values that are also listed in Table S2. It is noted that each E_{air} is much below the corresponding ΔE_k. Therefore, the first contribution E_p is dominant and can be calculated as $\Delta E_k - E_{air}$, see Table S2. By such subtraction, both v_i and v_r are corrected to the values just at the front and back sides of the nanofilm. Here, the deformation of the Al micro-particle is neglected. In fact, such particle deformation is beneficial to the impact resistance of the MG nanofilm.

During the present impacts, the diameter of the bullet-particle is much larger than the nanofilm's thickness, i.e., $D/h \gg 1$. In this situation, the wave propagation and energy dissipation can be neglected along the thickness direction of the nanofilm. Therefore, the penetration energy E_p can be further expressed as:

$$E_p = (\rho A_s h) \frac{v_i^2}{2} + E_d, \qquad (2)$$

where ρ is the density (13.168 g/cm^3) of the Ni$_{60}$Ta$_{40}$ MG nanofilm, and $A_s = \pi D^2/4$ is the strike-face area impacted by the spherical micro-particle. The first term on the right-hand side of Eq. (2) represents the kinetic energy transferred to the nanofilm within A_s and the second term E_d accounts for all other types of dissipated energy beyond A_s. In line with the work of Lee et al. [5], we normalized Eq. (2) by the mass within the strike-face body $A_s h$ and then obtained the specific penetration energy:

$$E_p^* = \frac{1}{2}v_i^2 + E_d^*, \qquad (3)$$

where $E_p^* = E_p (\rho A_s h)^{-1}$ characterizes the intrinsic impact-resistance of the MG nanofilms. Eq. (3) indicates that E_p^* can be decomposed into two contributions: the material-independent energy dissipation $\frac{1}{2}v_i^2$ and the delocalized penetration energy E_d^* dissipated outside the strike-face body $A_s h$. The E_d^* is generally material-dependent and also possibly a function of the impact velocity v_i. More importantly, the defined E_p^* allows a universal comparison of impact-resistance among different materials.

Fig. 4b plots the calculated E_p^* as a function of the impact velocity v_i for the Ni$_{60}$Ta$_{40}$ MG nanofilms. The data can be well fitted by Eq. (3) with $E_d^* = 3.5 \times 10^2 v_i + 2.5 \times 10^5$ as the red dashed curve in Fig. 4b. It is noted that the delocalized penetration energy E_d^* is linearly proportional to the impact velocity v_i. We find that the E_p^* data will seriously deviate from Eq. (3) if the E_d^* is fixed to be a constant, see the supplementary material, Fig. S2. For comparison, some typical bulk or ultrathin protective materials such as Q235 low carbon steel [11], 45 medium carbon steel [32], 304 stainless steel [33], Al [4], glassy poly(methyl methacrylate) (PMMA) [5,34], Kevlar armor [35], 24 nm thick gold film [5], multilayer graphene [5], graphene oxide-silk fibroin (GO-SF) nanocomposites [12], 75 nm thick polystyrene film [13], 200 nm thick polycarbonate film [14], and 73 nm thick P(VDF-TrFE) film [6] are also included in this plot. We find that all data reside in the region above a lower boundary (orange dashed curve) described by Eq. (3) with $E_d^* = 0$, i.e., $E_p^* = v_i^2/2$. This lower boundary as a benchmark means that the kinetic energy loss ΔE_k of the projectile completely dissipates within the strike-face body $A_s h$. The more the E_p^* data shift upward above this benchmark, the more the energy E_d^* dissipates outside $A_s h$. For crystalline metals (including gold nanofilms) and PMMA (a typical amorphous glassy polymer), their E_p^* data are up bounded by the blue dashed curve, that is, Eq. (3) with $E_d^* = 1.35 \times 10^2 v_i + 1.5 \times 10^5$. Compared with these impact-protective materials, the Ni$_{60}$Ta$_{40}$ MG nanofilms show the obvious superiority of the impact-resistance with higher E_p^* or E_d^*.

We also note that the E_p^* values for the Ni$_{60}$Ta$_{40}$ MG nanofilm and the so-called Kevlar armor [35] are very close at v_i of $\sim$300 and 400 m/s. Kevlar is known as an "armor-grade" composite, which consists of strong, stiff KM2 fibers as the reinforcement phase embedded in a PVB resin matrix. Such a highly complex structure results in the contribution of a large sample fraction and numerous frictional areas to impact energy absorption [35,36]. Furthermore, in terms of the E_p^* at $\sim$400 m/s, the MG nanofilm is comparable to some nacre-mimetic GO-SF nanocomposites [12] that use natural SF as a matrix reinforced by GO flakes. The high impact resistance of such nanocomposites arises from the GO-enhanced toughness and resulting long-distance propagation of stress waves. The high-velocity extrapolated value of the MG nanofilm is below most ultrathin polymer films [6,13,14] and multilayer graphene [5]. Under micro-projectile impacts, these ultrathin polymer films usually exhibit abundant viscoelastic and viscoplastic deformation modes prior to perforation and film rupture, while multilayer graphene undergo long-distance breaking
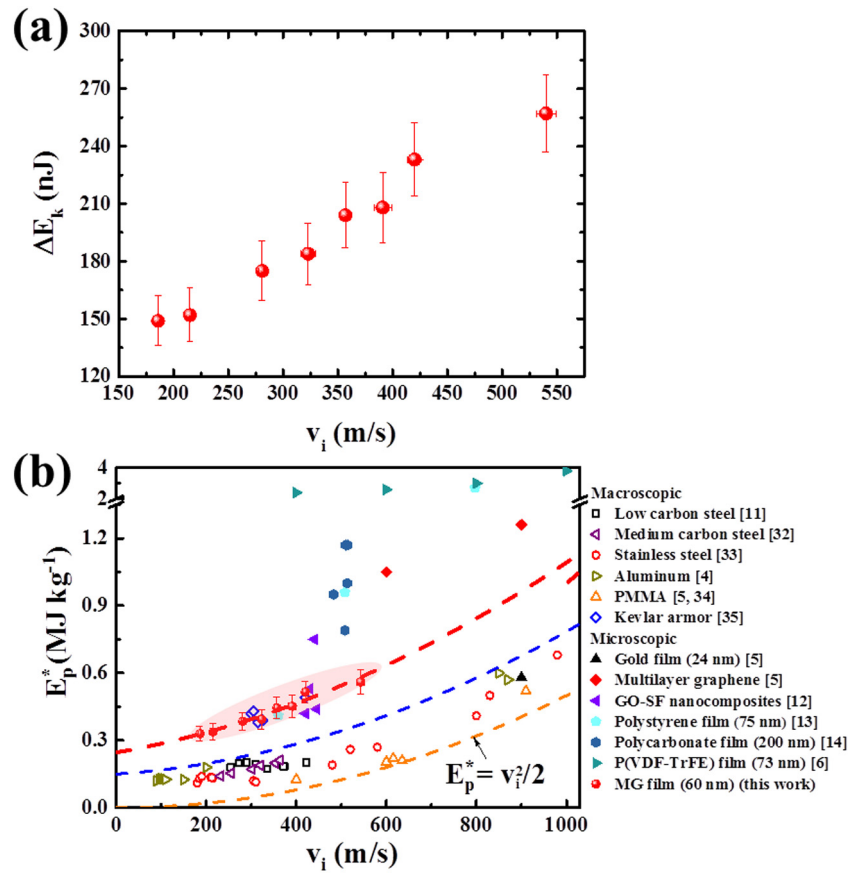
Fig. 4. Ballistic performance and energy analysis during penetration of the Al micro-particle into the $Ni_{60}Ta_{40}$ MG nanofilm. (a) The kinetic energy loss ΔE_k of the micro-particle versus its impact velocity v_i. (b) The specific penetration energy E_p^* for the $Ni_{60}Ta_{40}$ MG nanofilm in this study and other bulk or ultrathin impact-protective materials [4–6,11–14,31–34] as a function of v_i. The three dashed lines in (b) are all fitted by Eq. (3) with $E_d^* = 3.5 \times 10^2 v_i + 2.5 \times 10^5$(red), $E_d^* = 1.35 \times 10^2 v_i + 1.5 \times 10^5$ (blue) and $E_d^* = 0$ (orange), respectively. . (For interpretation of the references to color in this figure legend, the reader is referred to the web version of this article.)

of strong covalent bonding beyond perforated hole. Compared with the Kevlar armor and these nanostructured materials mentioned above, the present $Ni_{60}Ta_{40}$ MG nanofilm has a relatively simple configuration: a 60-nm-thick single-layer amorphous alloy and isotropic metallic bonding. More importantly, the MG nanofilms can be expediently fabricated on a large scale, along with controllable tuning of the chemical composition or feature thickness. It is expected that the impact-resistance of the MG nanofilm could be further enhanced by optimizing the chemical composition, the feature thickness or the number of layers.

The post-penetration features are further observed to uncover the dissipation modes of the impact energy for the $Ni_{60}Ta_{40}$ MG nanofilms. Three typical cases for the impact velocities v_i of 215 m/s, 420 m/s and 540 m/s are shown in Fig. 5, where the dashed circles denote the strike-face area A_s of the Al micro-particle. Obviously, all real damage areas are much larger than A_s, corresponding to the highly delocalized penetration energy E_d^*. By contrast, the materials below the blue dashed curve in Fig. 4b show a damage area close to A_s, implying that the impact energy dissipation is highly localized and corresponding to relatively low E_d^*. More importantly, both the damage area and the damage forms show a significant dependence on the impact velocity v_i for the present $Ni_{60}Ta_{40}$ MG nanofilm. The damage forms include: perforated hole, shear-banding, cracking, and bending of cracking-induced petals, which all contribute to the impact energy dissipation.

Fig. 5a–c show that the perforated holes become larger with increasing v_i. Multiple shear bands can be observed around the

perforated hole at 215 m/s; see Fig. 5a. A close-up observation of shear bands is shown in Fig. 5d. Such plastic dissipation is unique for MG nanofilms, since shear transformations (STs) as the basic flow events in MGs can occur at the nanoscale [37–39]. These observed shear bands result from localized self-organization of STs under the high strain rate loading. At 420 m/s; see Fig. 5b, many radial shear cracks occur around the perforated hole, which induces the creation of several petals. Fig. 5e shows a close-up view of a shear crack. These shear cracks are a consequence of shear-band propagation as strain rates increase [40]. We also observe the permanent bending of petals; see Fig. 5f, which indicates significant global plastic deformation in addition to the localized shear bands. This is a sharp contrast to the very limited plastic strain (less than 1%) of the bulk $Ni_{60}Ta_{40}$ MG [27]. At the highest velocity of 540 m/s, a higher number of radial cracks can be observed around the largest perforated hole; see Fig. 5c. These cracks also result from the development of shear bands. This is evidenced by the high-magnification TEM observations of shear bands ahead of the crack tip at the 540 m/s impact (the supplementary material, Fig. S3). Based on a constitutive model of amorphous plasticity developed previously by Jiang et al. [41], the underlying mechanism is the strain-rate effect of structural dynamics in MGs. At higher impact velocities or strain rates, higher levels of shear stress can be reached faster, which activates STs and resulting free volume creation more rapidly. The faster structural dynamics facilitate the nucleation of multiple shear bands at different sites [42,43]. Overall, the penetration features of the $Ni_{60}Ta_{40}$ MG nanofilms are similar to those reported for
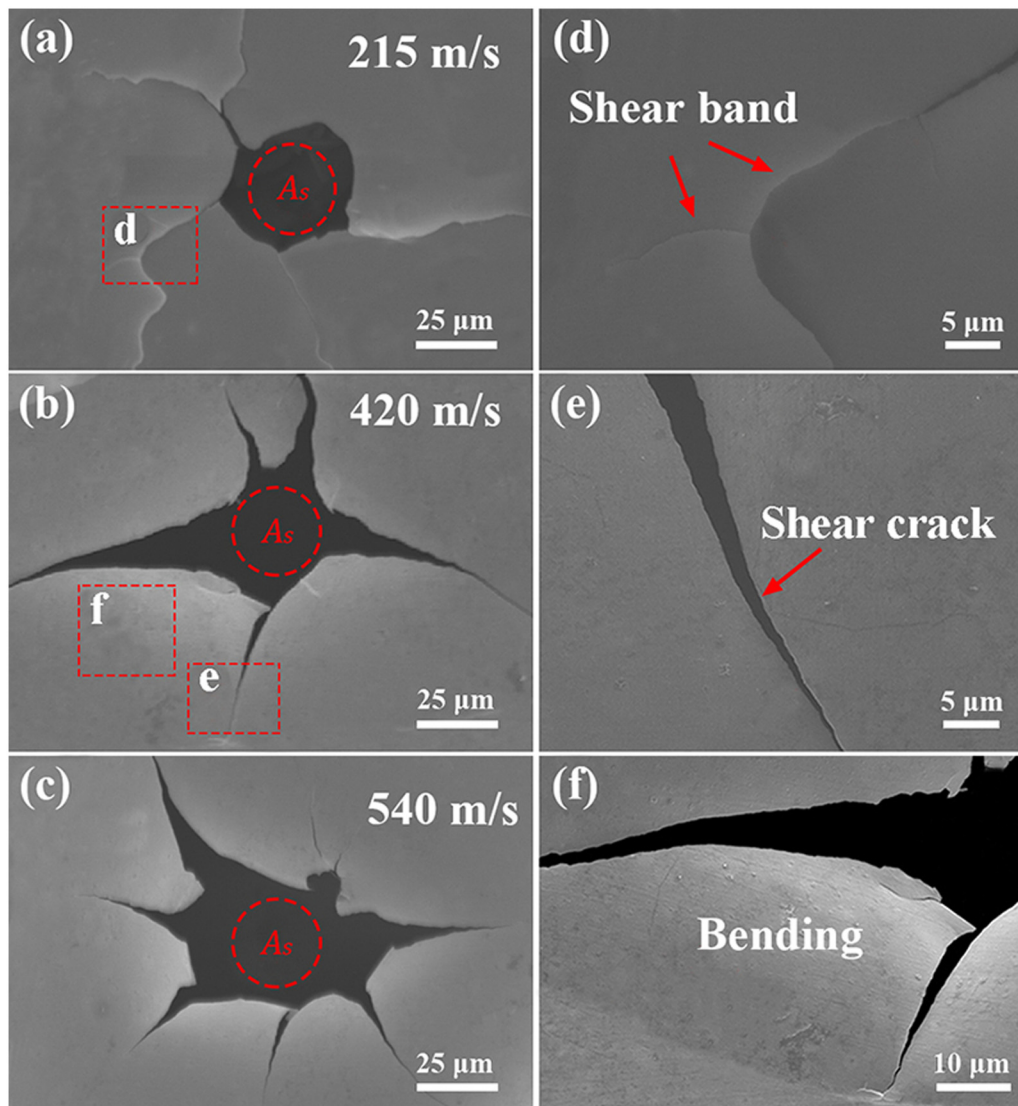
Fig. 5. Typical post-penetration features of the $Ni_{60}Ta_{40}$ MG nanofilm at impact velocities: (a) 215 m/s, (b) 420 m/s, and (c) 540 m/s. (d) A close-up view of the area "d" in (a). (e) and (f) A close-up view of the areas "e" and "f", respectively, in (b).

multilayer graphene [5] and GO-SF nanocomposites [12]. But the primary difference is that the cracks in the MG nanofilms are induced by plastic shear-banding, whereas in the latter the cracks formed according to brittle mode I breaking of covalent bonding. The plastic deformation ahead of crack tips, as an effective way to energy dissipation, contributes to the high E_p^* or E_d^* of the $Ni_{60}Ta_{40}$ MG nanofilms shown in Fig. 4b.

At last, we exclude the phase transformation mechanism for impact energy dissipation of the $Ni_{60}Ta_{40}$ MG nanofilms. The high-resolution TEM images and SAED patterns (the supplementary material, Fig. S4) confirm that the damage areas after penetration remain long-range disordered, glassy states, and no crystallization is detected. Based on a recent study of the crystallization kinetics of nanoscale MGs [44], the preservation of the glassy structure observed here should result from two interrelated reasons. First, the time window in the current high-velocity impact is much shorter than the time for the crystallization onset. Second, the high-strain-rate induced temperature rise within the nanofilms is not sufficiently high to initiate crystallization, because of the high thermal diffusivity along the thickness direction. The temperature rise is approximately estimated in the supplementary material. Indeed, we do not observe any heating or

melting phenomenon from the post-penetration patterns (Fig. 5) of the MG nanofilm in the tested velocity regime.

4. Conclusions

In this work, laser-induced micro-particle penetration experiments were performed on $Ni_{60}Ta_{40}$ MG nanofilms at different impact velocities. Based on the ballistic analysis, the specific penetration energy is analyzed to quantify the impact resistance of the MG nanofilms. We demonstrate that the MG nanofilms can effectively dissipate the impact energy via mechanical modes rather than phase transformation. Beyond the localized perforated holes, the diverse dissipation modes for impact energy include shear banding, cracking, and bending of cracking-induced petals, which depend on the impact velocity of the micro-particles.

According to the present study, one of the potential ballistic applications of MG nanofilms is the use as high-performance coating reinforcement. By the IBAD technique, MG nanofilms can be easily deposited on various substrates such as metals or alloys, polymers and silica. For example, it is intriguing to deposit a MG nanofilm to an ultrathin polymer film, and the fabricated multilayer composite-film is expected to achieve very high impact

resistance to micro- or macro-projectile impacts. Furthermore, in the impact protection scenarios at high temperatures, the present $Ni_{60}Ta_{40}$ MG nanofilms are of obvious advantages due to the very high glass transition temperature (about 1000 K) and melting point (larger than 1600 K) [27]. The polymer- or carbon-based protective materials in contrast cannot endure the high-temperature impacts. Thus, in addition to the use as projectile, as investigated about twenty years ago [45], MGs due to their unique mechanical response are also highly apt materials for impact protection.

Declaration of competing interest

The authors declare that they have no known competing financial interests or personal relationships that could have appeared to influence the work reported in this paper.

Acknowledgments

Appendix A. Supplementary data

Supplementary material related to this article can be found online at https://doi.org/10.1016/j.eml.2021.101258.

References

[1] H.G. Chae, S. Kumar, Making strong fibers, Science 319 (2008) 908–909.

[2] E. Grossman, I. Gouzman, R. Verker, Debris/micrometeoroid impacts and synergistic effects on spacecraft materials, MRS Bull. 35 (2010) 41–47.

[3] S. Xue, Z. Fan, O.B. Lawal, R. Thevamaran, Q. Li, Y. Liu, K.Y. Yu, J. Wang, E.L. Thomas, H. Wang, X. Zhang, High-velocity projectile impact induced 9R phase in ultrafine-grained aluminium, Nature Commun. 8 (2017) 1653.

[4] N.K. Gupta, M.A. Iqbal, G.S. Sekhon, Experimental and numerical studies on the behavior of thin aluminum plates subjected to impact by blunt- and hemispherical-nosed projectiles, Int. J. Impact Eng. 32 (2006) 1921–1944.

[5] J.-H. Lee, P.E. Loya, J. Lou, E.L. Thomas, Dynamic mechanical behavior of multilayer graphene via supersonic projectile penetration, Science 346 (2014) 1092–1096.

[6] J. Cai, R. Thevamaran, Superior energy dissipation by ultrathin semicrystalline polymer films under supersonic microprojectile impacts, Nano Lett. 20 (2020) 5632–5638.

[7] K. Mylvaganam, L.C. Zhang, Energy absorption capacity of carbon nanotubes under ballistic impact, Appl. Phys. Lett. 89 (2006) 123127.

[8] S.L. Phoenix, P.K. Porwal, A new membrane model for the ballistic impact response and V50 performance of multi-ply fibrous systems, Int. J. Solids Struct. 40 (2003) 6723–6765.

[9] J.H. Lee, D. Veysset, J.P. Singer, M. Retsch, G. Saini, T. Pezeril, K.A. Nelson, E.L. Thomas, High strain rate deformation of layered nanocomposites, Nature Commun. 3 (2012) 1164.

[10] O.E. Petel, S. Ouellet, J. Loiseau, B.J. Marr, D.L. Frost, A.J. Higgins, The effect of particle strength on the ballistic resistance of shear thickening fluids, Appl. Phys. Lett. 102 (2013) 064103.

[11] Y. Deng, W. Zhang, Z. Cao, Experimental investigation on the ballistic resistance of monolithic and multi-layered plates against hemispherical-nosed projectiles impact, Mater. Des. 41 (2012) 266–281.

[12] W. Xie, S. Tadepalli, S.H. Park, A. Kazemi-Moridani, Q. Jiang, S. Singamaneni, J.-H. Lee, Extreme mechanical behavior of nacre-mimetic graphene-oxide and silk nanocomposites, Nano Lett. 18 (2018) 987–993.

[13] J. Hyon, O. Lawal, O. Fried, R. Thevamaran, S. Yazdi, M. Zhou, D. Veysset, S.E. Kooi, Y. Jiao, M.-S. Hsiao, J. Streit, R.A. Vaia, E.L. Thomas, Extreme energy absorption in glassy polymer thin films by supersonic micro-projectile impact, Mater. Today 21 (2018) 817–824.

[14] E.P. Chan, W. Xie, S.V. Orski, J.-H. Lee, C.L. Soles, Entanglement density-dependent energy absorption of polycarbonate films via supersonic fracture, ACS Macro Lett. 8 (2019) 806–811.

[15] J. Schroers, W.L. Johnson, Ductile bulk metallic glass, Phys. Rev. Lett. 93 (2004) 255506.

[16] M.X. Li, S.F. Zhao, Z. Lu, A. Hirata, P. Wen, H.Y. Bai, M. Chen, J. Schroers, Y. Liu, W.H. Wang, High-temperature bulk metallic glasses developed by combinatorial methods, Nature 569 (2019) 99.

[17] T. Ju, H. Zhou, Pressure-induced maximum shear strength and transition from shear banding to uniform plasticity in metallic glass, Extrem. Mech. Lett. 41 (2020) 101058.

[18] X. Huang, Z. Ling, Z.D. Liu, H.S. Zhang, L.H. Dai, Amorphous alloy reinforced Whipple shield structure, Int. J. Impact Eng. 42 (2012) 1–10.

[19] D.C. Hofmann, L. Hamill, E. Christiansen, S. Nutt, Hypervelocity impact testing of a metallic glass-stuffed whipple shield, Adv. Eng. Mater. 17 (2015) 1313–1322.

[20] M. Davidson, S. Roberts, G. Castro, R.P. Dillon, A. Kunz, H. Kozachkov, M.D. Demetriou, W.L. Johnson, S. Nutt, D.C. Hofmann, Investigating amorphous metal composite architectures as spacecraft shielding, Adv. Eng. Mater. 15 (2013) 27–33.

[21] L. Hamill, S. Roberts, M. Davidson, W.L. Johnson, S. Nutt, D.C. Hofmann, Hypervelocity impact phenomenon in bulk metallic glasses and composites, Adv. Eng. Mater. 16 (2014) 85–93.

[22] H. Guo, P.F. Yan, Y.B. Wang, J. Tan, Z.F. Zhang, M.L. Sui, E. Ma, Tensile ductility and necking of metallic glass, Nature Mater. 6 (2007) 735–739.

[23] L. Tian, Y.Q. Cheng, Z.W. Shan, J. Li, C.C. Wang, X.D. Han, J. Sun, E. Ma, Approaching the ideal elastic limit of metallic glasses, Nature Commun. 3 (2012) 609.

[24] G. Kumar, A. Desai, J. Schroers, Bulk metallic glass: the smaller the better, Adv. Mater. 23 (2011) 461–476.

[25] D. Jang, J.R. Greer, Transition from a strong-yet-brittle to a stronger-and-ductile state by size reduction of metallic glasses, Nature Mater. 9 (2010) 215–219.

[26] S. Adibi, P.S. Branicio, R. Liontas, D.Z. Chen, J.R. Greer, D.J. Srolovitz, S.P. Joshi, Surface roughness imparts tensile ductility to nanoscale metallic glasses, Extrem. Mech. Lett. 5 (2015) 88–95.

[27] Y. Wang, Q. Wang, J. Zhao, C. Dong, Ni–Ta binary bulk metallic glasses, Scr. Mater. 63 (2010) 178–180.

[28] D. Veysset, A.J. Hsieh, S. Kooi, A.A. Maznev, K.A. Masser, K.A. Nelson, Dynamics of supersonic microparticle impact on elastomers revealed by real–time multi–frame imaging, Sci. Rep. 6 (2016) 25577.

[29] J.H. Lee, D. Veysset, J.P. Singer, M. Retsch, G. Saini, T. Pezeril, K.A. Nelson, E.L. Thomas, High strain rate deformation of layered nanocomposites, Nat. Commun. 3 (2012) 1164.

[30] M. Hassani-Gangaraj, D. Veysset, K.A. Nelson, C.A. Schuh, Melting can hinder impact-induced adhesion, Phys. Rev. Lett. 119 (2017) 175701.

[31] M. Hassani-Gangaraj, D. Veysset, K.A. Nelson, C.A. Schuh, Melt-driven erosion in microparticle impact, Nature Commun. 9 (2018) 5077.

[32] Y.F. Deng, W. Zhang, G.H. Qing, G. Wei, Y.G. Yang, P. Hao, The ballistic performance of metal plates subjected to impact by blunt-nosed projectiles of different strength, Mater. Des. 54 (2014) 1056–1067.

[33] J. Dean, C.S. Dunleavy, P.M. Brown, T.W. Clyne, Energy absorption during projectile perforation of thin steel plates and the kinetic energy of ejected fragments, Int. J. Impact Eng. 36 (2009) 1250–1258.

[34] L.H. Abbud, A.R.A. Talib, F. Mustapha, H. Tawfique, F.A. Najim, Behaviour of transparent_material under high velocity impact, JSME Int. J. A 5 (2010) 123–128.

[35] B.L. Lee, T.F. Walsh, S.T. Won, H.M. Patts, J.W. Song, A.H. Mayer, Penetration failure mechanismsof armor-grade fibercomposites under impact, J. Compos. Mater. 35 (2001) 1605–1633.

[36] M. Cheng, W.N. Chen, T. Weerasooriya, Experimental investigation of the transverse mechanical properties of a single Kevlar? KM2 fiber, Int. J. Solids Struct. 41 (2004) 6215–6232.

[37] C.A. Schuh, T.C. Hufnagel, U. Ramamurty, Mechanical behavior of amorphous alloys, Acta Mater. 55 (2007) 4067–4109.

[38] M.L. Falk, J.S. Langer, Dynamics of viscoplastic deformation in amorphous solids, Phys. Rev. E 57 (1998) 7192–7205.

[39] D. Pan, A. Inoue, T. Sakurai, M.W. Chen, Experimental characterization of shear transformation zones for plastic flow of bulk metallic glasses, Proc. Natl. Acad. Sci. USA 105 (2008) 14769–14772.

[40] F. Zeng, M.Q. Jiang, L.H. Dai, Dilatancy induced ductile–brittle transition of shear band in metallic glasses, Proc. R. Soc. Lond. Ser. A Math. Phys. Eng. Sci. 474 (2018) 20170836.

[41] M.Q. Jiang, G. Wilde, L.H. Dai, Origin of stress overshoot in amorphous solids, Mech. Mater. 81 (2015) 72–83.

[42] M.Q. Jiang, L.H. Dai, On the origin of shear banding instability in metallic glasses, J. Mech. Phys. Solids 57 (2009) 1267–1292.

[43] M.Q. Jiang, S.Y. Jiang, Z. Ling, L.H. Dai, Smaller Deborah number inducing more serrated plastic flow of metallic glass, Comput. Mater. Sci. 46 (2009) 767–771.

[44] W. Yan, I. Richard, G. Kurtuldu, N.D. James, G. Schiavone, J.W. Squair, T. Nguyen-Dang, T. Das Gupta, Y. Qu, J.D. Cao, R. Ignatans, S.P. Lacour, V. Tileli, G. Courtine, J.F. Löffler, F. Sorin, Structured nanoscale metallic glass fibres with extreme aspect ratios, Nature Nanotechnology 15 (2020) 875–882.

[45] R.D. Conner, R.B. Dandliker, V. Scruggs, W.L. Johnson, Dynamic deformation behavior of tungsten-fiber/metallic glass matrix composites, Int. J. Impact Eng. 24 (2000) 435–444.